Science Advances
AAAS

advances.sciencemag.org/cgi/content/full/5/1/eaau3669/DC1

Supplementary Materials for

Delivery of carbon, nitrogen, and sulfur to the silicate Earth by a giant impact

Damanveer S. Grewal*, Rajdeep Dasgupta*, Chenguang Sun, Kyusei Tsuno, Gelu Costin

*Corresponding author. Email: dsg10@rice.edu (D.S.G.); rajdeep.dasgupta@rice.edu (R.D.)

Published 23 January 2019, *Sci. Adv.* **5**, eaau3669 (2019)
DOI: 10.1126/sciadv.aau3669

This PDF file includes:

Table S4. Major element compositions (in wt %) of the alloy melts at 1 to 7 GPa.
Table S5. Major element compositions (in wt %) of the silicate melts at 1 to 7 GPa.
References (*68–73*)

SUPPLEMENTARY MATERIALS

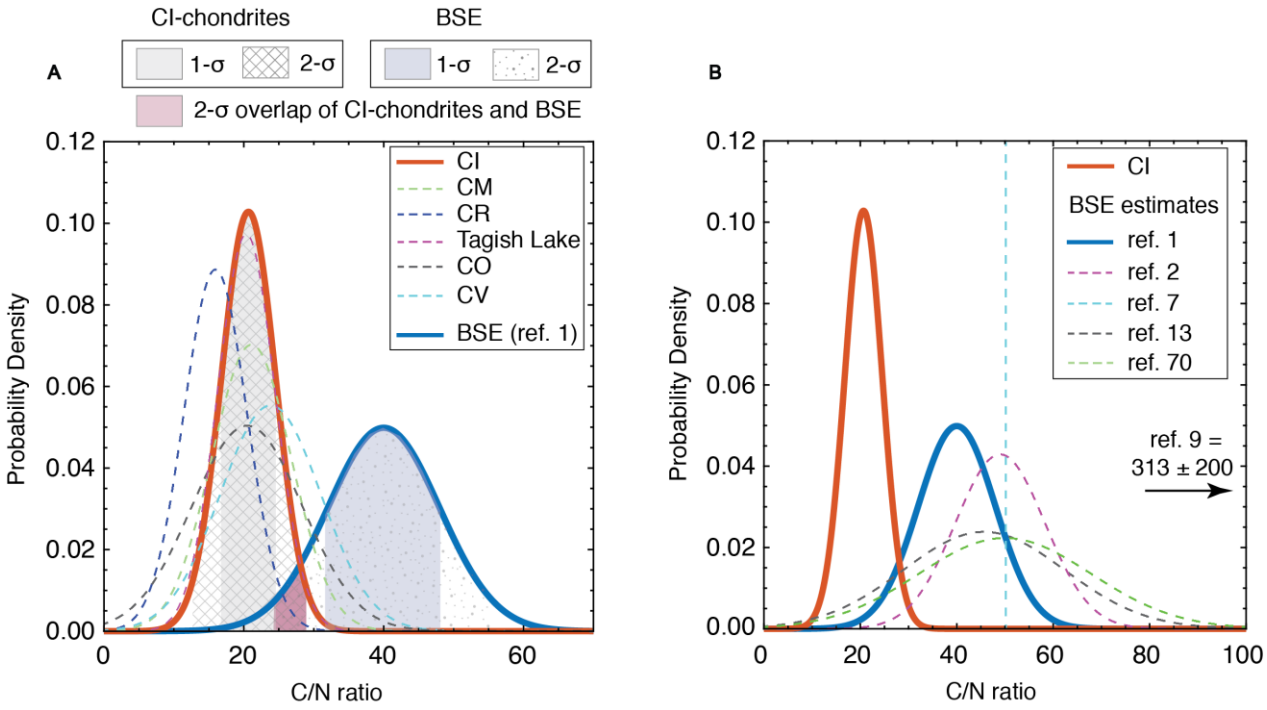

Fig. S1. Comparison between the estimated C/N ratios of the BSE and measured C/N ratios of CI and other carbonaceous chondrites. (A) The average C/N ratio of the BSE along with its standard deviation (*1*) is compared with the average C/N ratio of CI-chondrites along with its standard deviation via Gaussian probability distribution functions. The average C/N ratio of the BSE is distinctly greater than the average C/N ratio of CI-chondrites with no statistical overlap within a 1-σ range while there is a small but statistically insignificant overlap (~0.05 probability density area) within a 2-σ range. Probability density functions for other classes of carbonaceous chondrites are also plotted for comparison. (For details see table S1; carbonaceous chondrite compositional data is from (*68*, *69*)). **(B)** Probability density functions for all previous estimates (*1*, *2*, *7*, *9*, *13*, *70*) of the C/N ratio of the BSE are compared with the C/N ratio of CI-chondrites. The average C/N ratios of the BSE from all literature estimates are distinctly greater than the average C/N ratio of CI-chondrites.

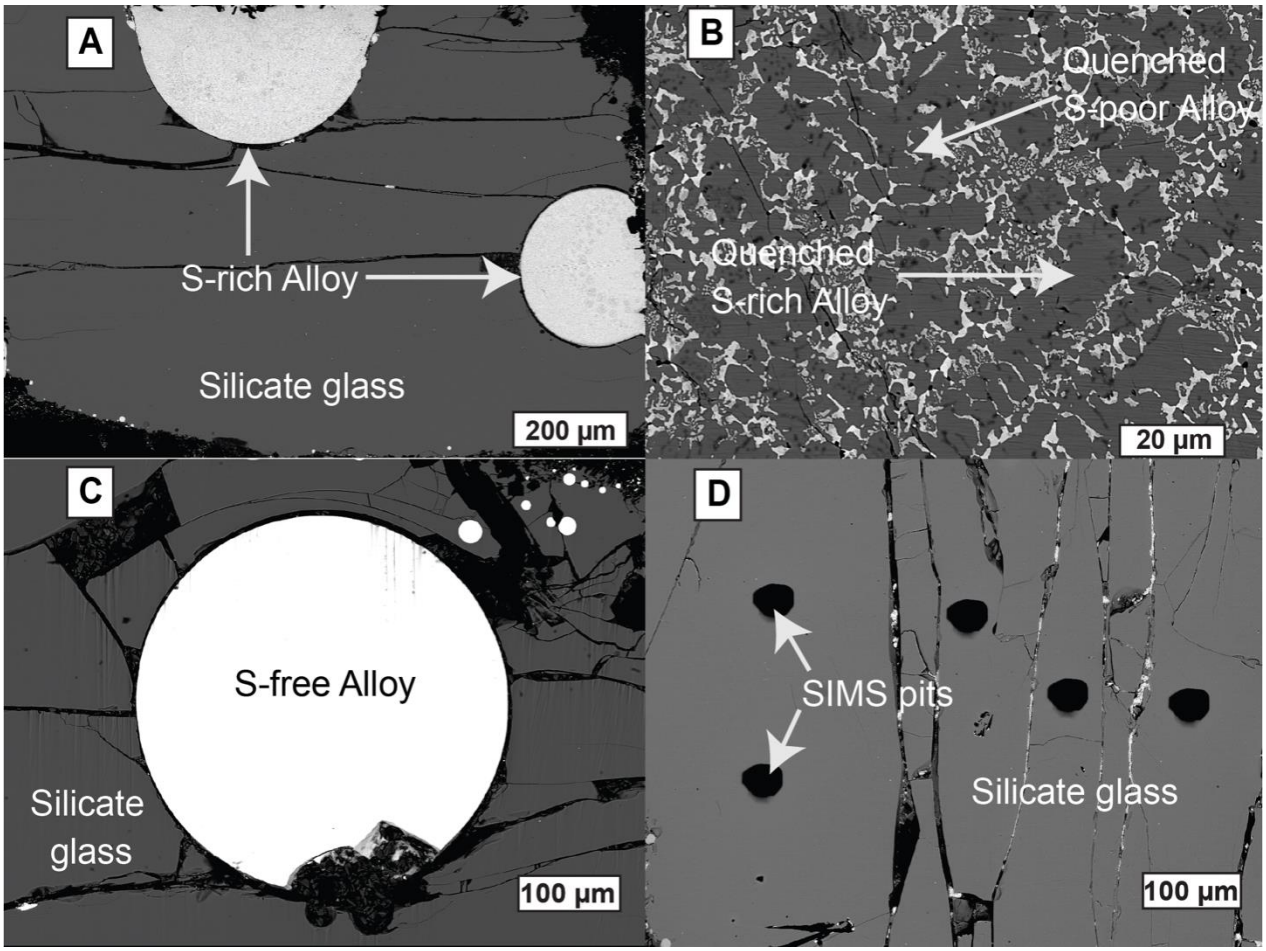

Fig. S2. Backscattered electron images of typical experimental products. (A) Coexistence of metallic alloy melt blobs and quenched silicate glass at 2 GPa-1600 °C with ~12 wt.% S in Fe-Ni alloy **(G503-10S)**. **(B)** Textures of quenched S-poor alloy (bright) and S-rich alloy (dark) phases at 3 GPa, 1600 °C with ~27 wt.% S in Fe-Ni alloy melt **(G491-20S)**. (**C)** Coexistence of metallic alloy melt blobs and quenched silicate glass at 2 GPa-1600 °C with an S-free Fe-Ni alloy **(G516-0S)**. **(D)** SIMS pits in a silicate glass **(G496-10S)**.

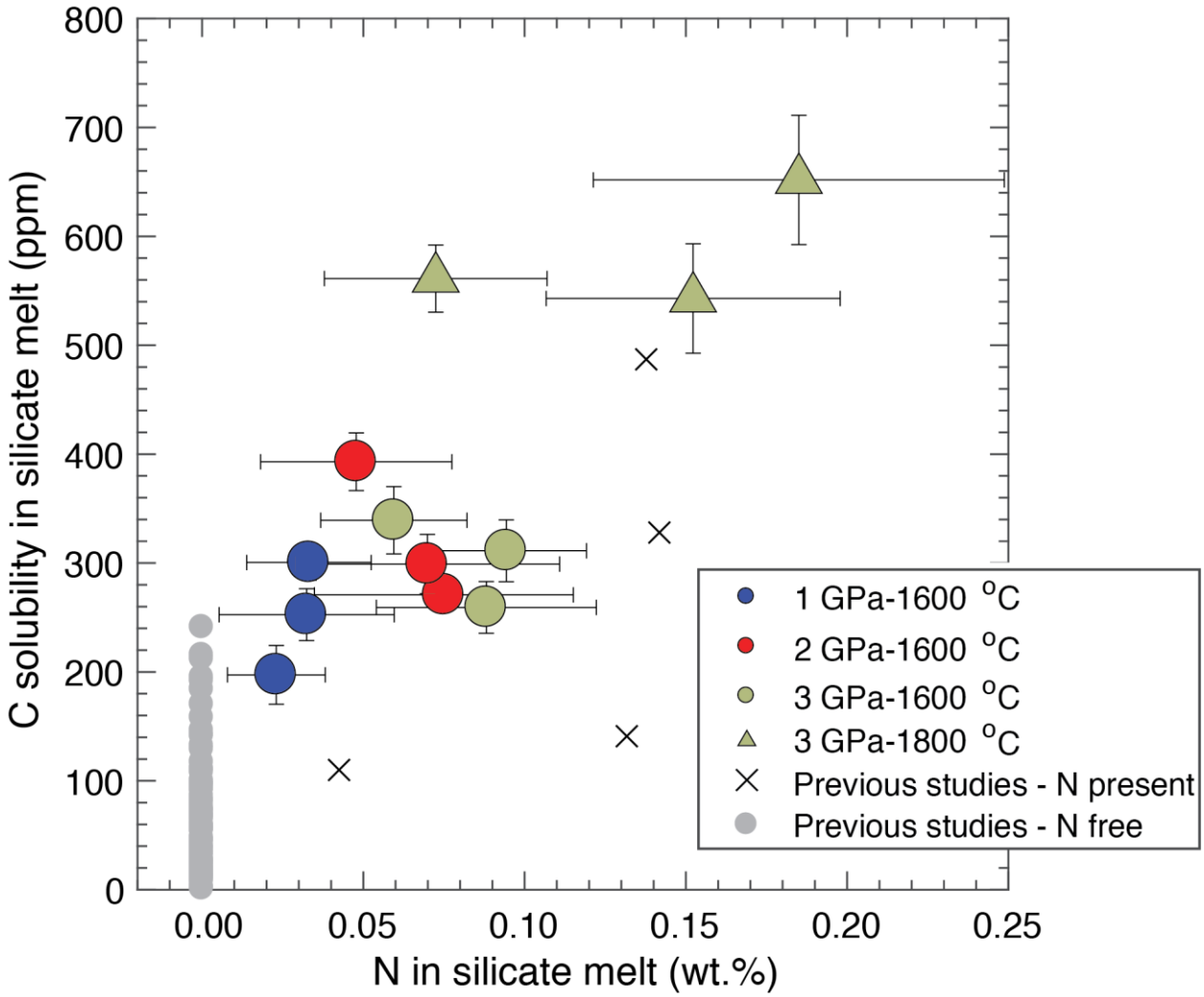

Fig. S3. Experimentally determined C solubility of the silicate melt at graphite saturation as a function of N content of the silicate melt. The C solubility in the silicate melt shows a positive correlation with the N content in the silicate melt. Both the N and C contents in the silicate melt show a positive correlation with *P* while the series of experiments conducted at 1800 °C have almost double the C and N contents that low *T* data have. The C solubility in an N-free system (*3*, *4*, *14*, *24*, *25*, *56*, *57*) is lower than in an N-present system in this study and previous studies (*12*), potentially owing to the formation of CN complexes as corroborated by the Raman spectra (fig. S4). Error bars are 1-σ and, if absent, are smaller than the symbol size.

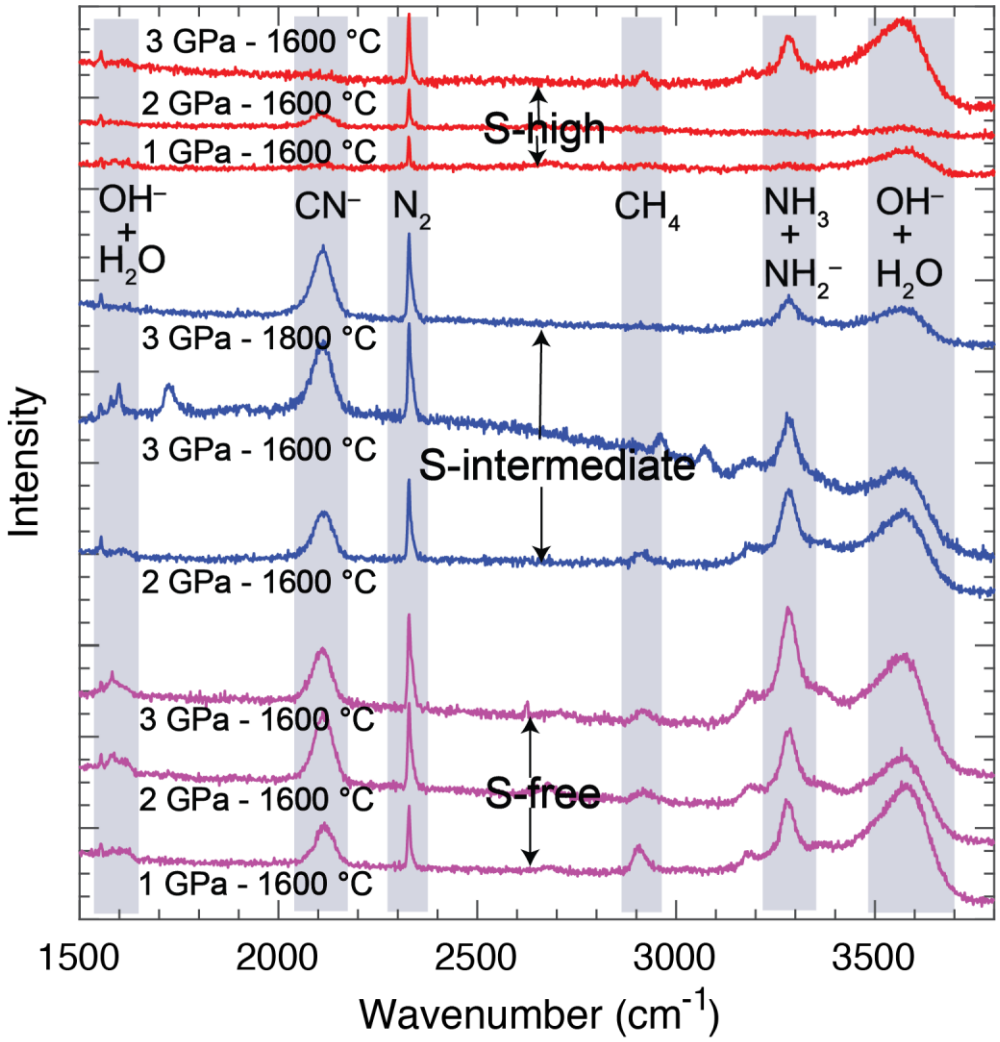

Fig. S4. Raman spectra of the experimental silicate glasses from this study showing peaks associated with C-O-N-H volatile species. Isolated N_2 molecules, N-H complexes, such as NH_3 and NH_2^-, CN^- complexes, isolated CH_4 molecules and OH^- + H_2O are the predominant dissolved volatiles species detected in our glasses. (For detailed discussion, see Methods Section).

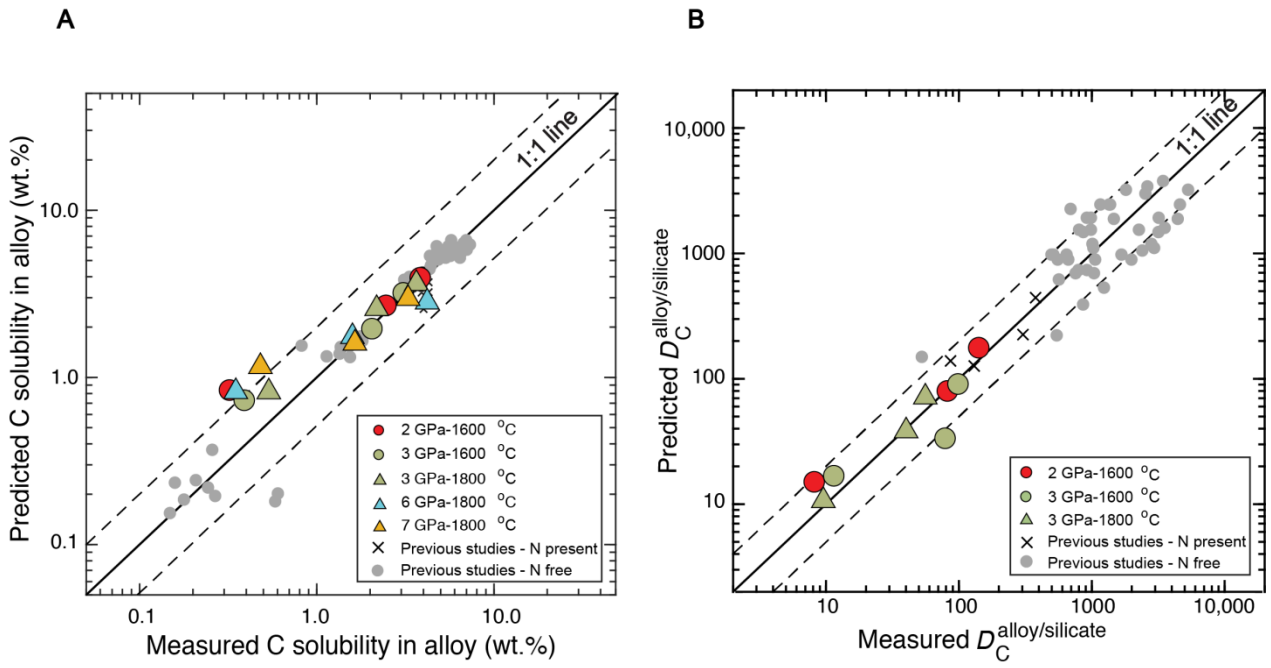

Fig. S5. Comparison between experimentally measured C solubility in the alloy melt and the $D_C^{alloy/silicate}$ and the predicted C solubility in the alloy melt and the $D_C^{alloy/silicate}$ based on the parameterizations developed in this study. (A) The C solubility in the alloy melt (wt.%) from the present study and previous studies (*3*, *4*, *12*, *14*, *24*, *25*) versus values predicted using Eq. 3. **(B)** The $D_C^{alloy/silicate}$ values from the present study and previous studies (*3*, *4*, *12*, *14*, *24*, *25*) versus those predicted using Eq. 4.

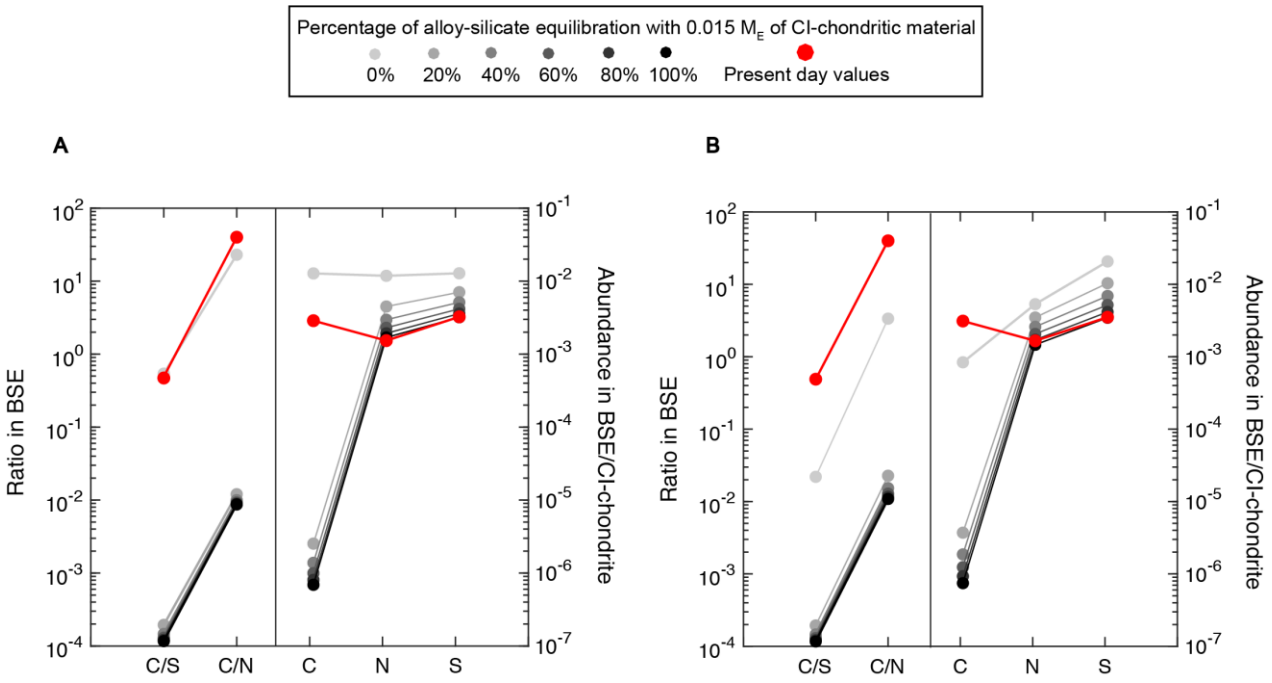

Fig. S6. Application of the experimental and parameterized alloy/silicate partition coefficients to examine whether a single-stage core formation along with an early atmospheric loss can explain the present-day abundances and ratios of C, N, and S in the BSE. (A) If the volatile bearing material, delivered by a 0.015-M_E of CI chondrites (*32*, *71*), did not equilibrate with the core-forming alloy (i.e., was delivered primarily as a late veneer), then the present-day superchondritic C/N ratio of the BSE cannot be attained, and the abundances of the volatiles would be much higher than in the present-day BSE. With an increase in the percentage of volatile participation in an alloy-silicate equilibration with an S-poor alloy (~2 wt.% S), C is depleted more in the silicate MO relative to N and S (due to C being more siderophile than N and S) leading to the sub-present-day abundances of C in the BSE as well as sub-chondritic C/N and C/S ratios. **(B)** Here, loss of an early atmosphere formed due to MO degassing is considered along with a single-stage core formation. Under the relevant fO_2 conditions, the solubility of C at MO conditions is less than that of N and S (*1*, *53*, *56*, *61*). Therefore, C would be much more enriched in the early atmosphere relative to N and S. Accordingly, loss of an early atmosphere component

would deplete the resulting BSE in C, resulting in sub-chondritic C/N and C/S ratios. (For details, see Methods Section).

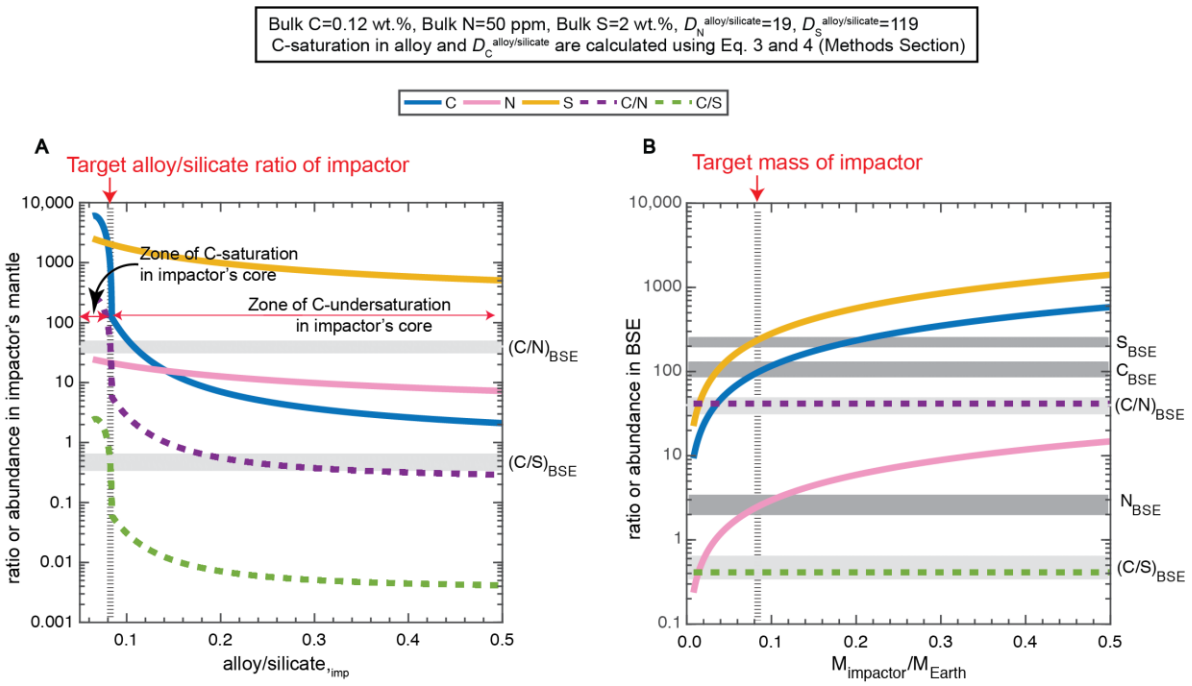

Fig. S7. An example forward calculation to showcase the methodology used to determine the alloy/silicate ratio and the mass of the impactor for a successful inverse Monte Carlo simulation. (A) Alloy-silicate partitioning dictates the abundances of N and S in the impactor's mantle, while either alloy-silicate partitioning alone or C-saturation in the alloy along with alloy-silicate partitioning dictate(s) the abundance of C as well as the C/N and C/N ratios. As shown in the above plot, when C saturation in the impactor's core is attained, the curve representing the C abundance in the impactor's mantle (solid blue) abruptly changes slope, which indirectly affects the slopes of the C/N and C/S curves (dashed purple and green, respectively). The match of the modelled C/N and C/S ratios in the impactor's mantle with the values in the present-day BSE (light grey areas) dictates the desirable alloy/silicate ratio of the impactor. Note that the alloy/silicate ratio of the impactor for this example calculation lies in the C-saturation zone. **(B)** After the merger of the volatile-bearing impactor with a volatile-free proto-Earth, the present-day abundances of C, N, and S in the BSE (dark grey areas) dictate the target mass ratio of the impactor.

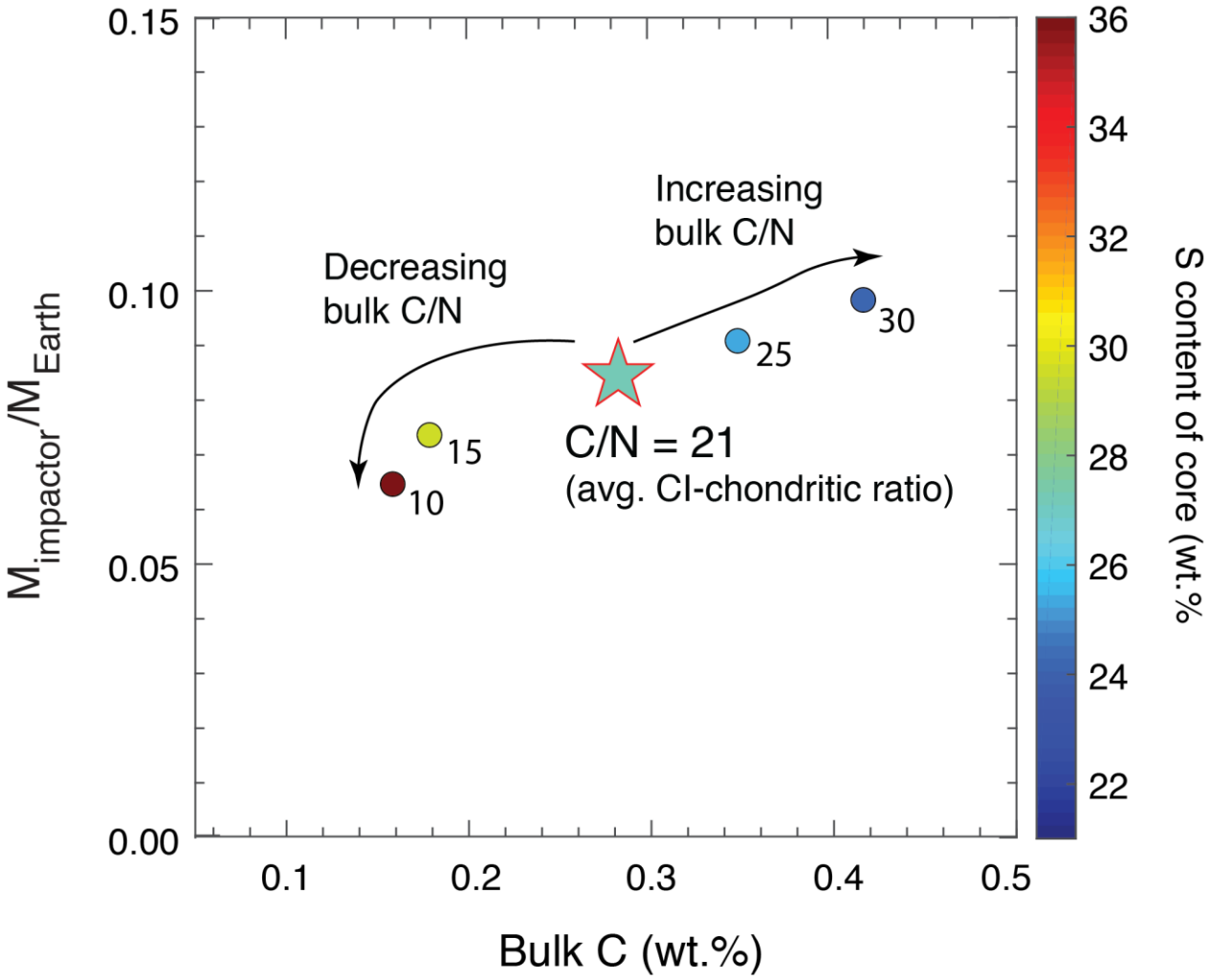

Fig. S8. Effect of varying bulk C/N ratios on the composition and the mass of the impactor, which could establish the C-N-S budget of the present-day BSE. A lower than average CI-chondritic C/N ratio (~21) of the accreting material leads to a decrease in the bulk C content and the mass of the impactor and an increase in the S content of the impactor's core, while a higher than average CI-chondritic C/N ratio of accreting material leads to an increase in the bulk C content and the mass of the impactor and decrease in the S content of the impactor's core. The bulk C/N is varied over a 1-σ range of all classes of carbonaceous chondrites.

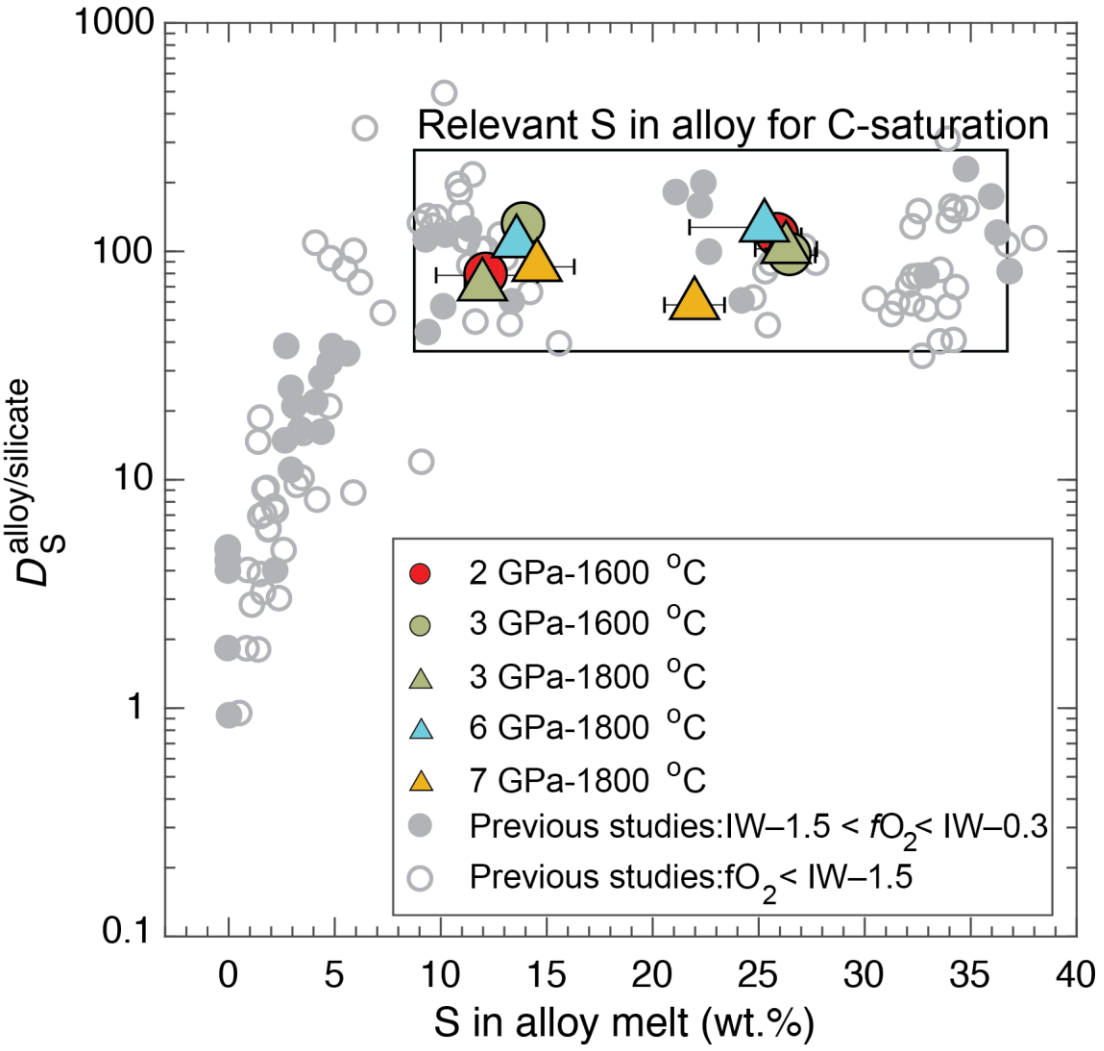

Fig. S9. Measured partition coefficients of S between the alloy and silicate melt as a function of S in the alloy melt. The $D_S^{alloy/silicate}$ increases with an increasing S content in the alloy (upto ~10 wt.% S in the alloy), whereas it does not change significantly between 10 and 36 wt.% S (marked by a box) in the alloy. To achieve C enrichment in the mantle of the impactor via C saturation in the alloy requires >10 wt.% S in our simulations, because, for <10 wt.% S in the alloy, a low $D_S^{alloy/silicate}$ would require a superchondritic bulk S in order to have sufficient S content in the alloy. The data represented by empty grey circles (*44*, *72*, *73*) lies in a lower fO_2 range than that which is relevant for our simulations. Therefore, the data represented by colored symbols and filled grey circles (*3*, *4*, *14*), lying in a limited fO_2 range, is used in our simulations. Additionally, the $D_S^{alloy/silicate}$ data relevant for a deep MO on the Earth (*30*) is not plotted here because the

$D_S^{alloy/silicate}$ values in this figure are used to model the core formation in a small planetary embryo.

Error bars are 1-σ and, if absent, are smaller than the symbol size.

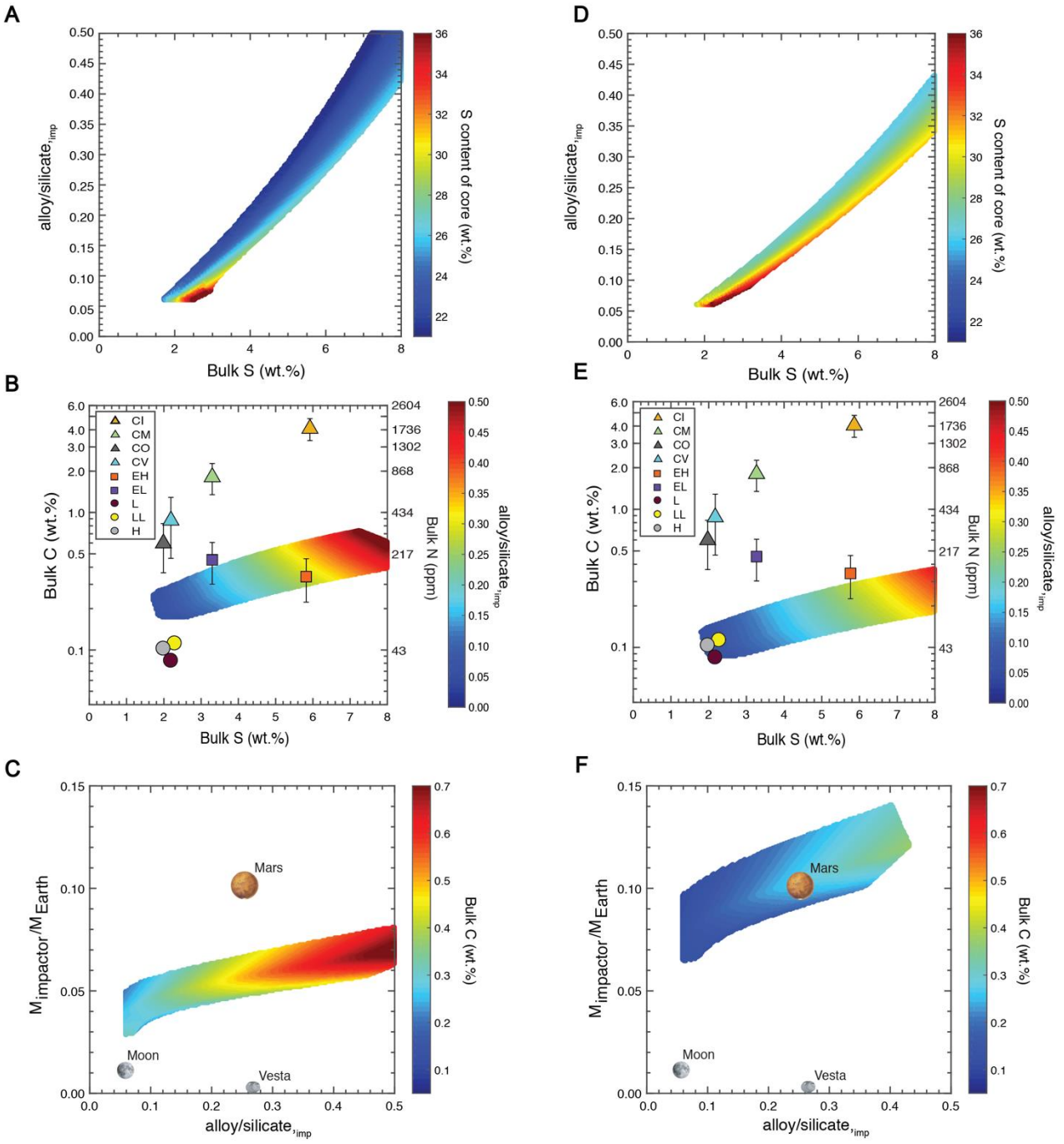

Fig. S10. Results of inverse Monte Carlo simulations to obtain the composition and mass of the impactor with end-member $D_S^{alloy/silicate}$ values. Results of inverse Monte Carlo simulations used to obtain the composition of the impactor with a low $D_S^{alloy/silicate}$ = 73 (**A**, **B**, **C**) and high $D_S^{alloy/silicate}$ = 165 (**D**, **E**, **F**). **(A)** The S content in the core of the impactor lies in a lower range in comparison to Fig. 4B. **(B)** The bulk C content of the impactor lies in a higher range in comparison to Fig. 4C. **(C)** The mass of the impactor is distinctly lower in comparison to Fig. 4D

because of the higher abundances of volatiles in the mantle of the impactor due to higher bulk concentrations of C, N and S. **(D)** The S content in the core of the impactor lies in a higher range in comparison to Fig. 4B. **(E)** The bulk C content of the impactor lies in a lower range in comparison to Fig. 4C. **(F)** The mass of the impactor is distinctly higher in comparison to Fig. 4D because of the lower abundances of volatiles in the mantle of the impactor due to lower bulk concentrations of C, N and S.

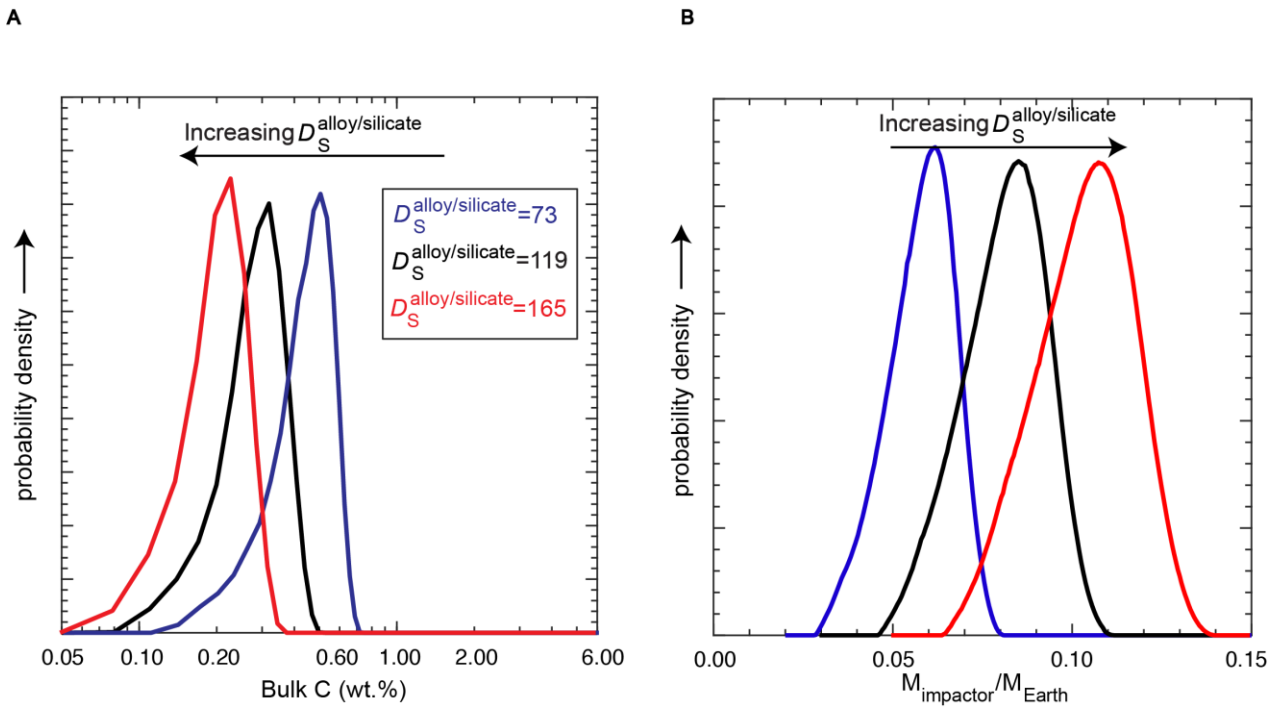

Fig. S11. Results of inverse Monte Carlo simulations showing the effect of a variable $D_S^{alloy/silicate}$ on the estimated bulk C content and the mass of the impactor. (A) The most probable bulk C content (wt.%) of the impactor, as shown by the peaks, decreases with an increasing $D_S^{alloy/silicate}$. **(B)** The most probable mass of the impactor with respect to the present-day Earth's mass increases with an increasing $D_S^{alloy/silicate}$ (See Methods for detailed discussion).

Table S1. Comparison between the estimated C/N ratios of CI and other carbonaceous chondrites with that estimated for the BSE.

Carbonaceous chondrites		C/N ratio		Overlap with C/N ratio of BSE (ref. 1)	
	n	Mean	1-σ	1-σ	2-σ
CI	6	20.66	3.88	0.00	0.05
CV	5	23.82	7.21	0.00	0.22
CO	7	20.47	7.92	0.00	0.17
CM	72	21.09	5.68	0.00	0.12
Tagish Lake	3	20.35	4.10	0.00	0.05
CR	13	15.93	4.50	0.00	0.01
BSE estimates		C/N ratio		Overlap with C/N ratio of CI chondrites	
		Mean	1-σ	1-σ	2-σ
ref. 1		40.00	8.00	0.00	0.05
ref. 2		49.00	9.30	0.00	0.00
ref. 7		50.00	-	-	-
ref. 9		313.10	200.32	0.00	0.02
ref. 13		45.63	16.73	0.05	0.13
ref. 70		50.00	17.86	0.00	0.08

n is the number of distinct specimens for which measurements are averaged; data from refs. 68 and 69.
*The overlaps represent the probability density area of the overlap, e.g., 0.05 probability density area overlap within a 2-σ range (95% confidence interval) means that there is a 5% area overlap over the 2-σ range for the C/N ratio of the BSE and a given class of carbonaceous chondrites.

Table S2. Chemical compositions of the starting materials (in wt %).

ThB1	SiO_2	Al_2O_3	Cr_2O_3	FeO	MnO
	51.19	16.12	0.03	9.18	0.23
	MgO	CaO	Na_2O	K_2O	
	8.75	11.35	3.05	0.1	
Alloy mix	Fe	Ni	N	S	
Fe-5Ni-5N-0S	90	5	5	0	
Fe-5Ni-5N-10S	80	5	5	10	
Fe-5Ni-5N-20S	70	5	5	20	

ThB1, a TiO_2 free synthetic tholeiite basalt (ThB1), similar to the composition of a natural tholeiite basalt (ThB), used in several previous high-pressure alloy-silicate partitioning experimental studies was used as the silicate fraction of our starting mixes.

Table S3. Summary of the experimental conditions, quench products, oxygen fugacity, and alloy-silicate partitioning coefficients of C, N, and S.

Exp No.	*P* (GPa)	*T* (°C)	[a]Duration (mins)	[b]Starting materials	Quench products	[c]log fO_2 (ΔIW) Ideal	[d]log fO_2 (ΔIW) Non-ideal	Raman	$D_C^{alloy/silicate}$ Mean	(1-σ)	$D_N^{alloy/silicate}$ Mean	(1-σ)	$D_S^{alloy/silicate}$ Mean	(1-σ)
G517-0S	1	1600	60	ThB1+Fe-Ni(5wt.%)-N(5wt.%)	Glass+Alloy	-1.76	-1.17	✓	150.82	15.45	15.67	9.46	n.a.	n.a.
G516-0S	2	1600	120	ThB1+Fe-Ni(5wt.%)-N(5wt.%)	Glass+Alloy	-1.64	-1.06	✓	143.16	9.75	22.39	12.03	n.a.	n.a.
G498-0S	3	1600	120	ThB1+Fe-Ni(5wt.%)-N(5wt.%)	Glass+Alloy	-1.60	-1.06	✓	99.92	10.31	27.61	7.29	n.a.	n.a.
G499-0S	3	1800	20	ThB1+Fe-Ni(5wt.%)-N(5wt.%)	Glass+Alloy	-1.64	-1.06	✓	55.91	6.28	13.06	4.60	n.a.	n.a.
MA176-0S	6	1800	15	ThB1+Fe-Ni(5wt.%)-N(5wt.%)	Fine quench crystals+Alloy	-1.49	-0.83	×	n.a.	n.a.	31.16	10.43	n.a.	n.a.
MA184-0S	7	1800	15	ThB1+Fe-Ni(5wt.%)-N(5wt.%)	Fine quench crystals+Alloy	-1.50	-0.99	×	n.a.	n.a.	18.29	5.42	n.a.	n.a.
G504-10S	1	1600	60	ThB1+Fe-Ni(5wt.%)-N(5wt.%)-S(10wt.%)	Glass+Immiscible alloys	n.a.	n.a.	✓	n.a.	n.a.	n.a.	n.a	n.a.	n.a
G503-10S	2	1600	120	ThB1+Fe-Ni(5wt.%)-N(5wt.%)-S(10wt.%)	Glass+Alloy	-1.51	-1.05	✓	83.08	10.97	23.88	14.14	78.55	15.62
G493-10S	3	1600	120	ThB1+Fe-Ni(5wt.%)-N(5wt.%)-S(10wt.%)	Glass+Alloy	-1.43	-1.01	✓	79.86	7.64	29.00	11.28	130.48	8.57
G496-10S	3	1800	20	ThB1+Fe-Ni(5wt.%)-N(5wt.%)-S(10wt.%)	Glass+Alloy	-1.41	-0.97	✓	40.10	4.32	15.05	4.58	70.44	5.52
MA176-10S	6	1800	15	ThB1+Fe-Ni(5wt.%)-N(5wt.%)-S(10wt.%)	Fine quench crystals+Alloy	-1.36	-0.97	×	n.a.	n.a.	23.28	7.21	108.84	12.00
MA184-10S	7	1800	15	ThB1+Fe-Ni(5wt.%)-N(5wt.%)-S(10wt.%)	Fine quench crystals+Alloy	-1.29	-0.92	×	n.a.	n.a.	20.60	4.96	85.55	11.69
G515-20S	1	1600	60	ThB1+Fe-Ni(5wt.%)-N(5wt.%)-S(20wt.%)	Glass+Immiscible alloys	n.a.	n.a.	✓	n.a.	n.a.	n.a.	n.a	n.a.	n.a
G514-20S	2	1600	120	ThB1+Fe-Ni(5wt.%)-N(5wt.%)-S(20wt.%)	Glass+Alloy	-1.47	-1.71	✓	8.27	1.58	15.41	10.26	117.21	6.51
G491-20S	3	1600	120	ThB1+Fe-Ni(5wt.%)-N(5wt.%)-S(20wt.%)	Glass+Alloy	-1.03	-1.31	✓	11.61	3.30	15.38	6.09	96.19	4.70
G495-20S	3	1800	20	ThB1+Fe-Ni(5wt.%)-N(5wt.%)-S(20wt.%)	Glass+Alloy	-1.17	-1.32	✓	9.55	2.17	13.07	6.51	102.45	15.48
MA176-20S	6	1800	15	ThB1+Fe-Ni(5wt.%)-N(5wt.%)-S(20wt.%)	Fine quench crystals+Alloy	-1.12	-1.29	×	n.a.	n.a.	11.02	5.40	127.49	19.87
MA184-20S	7	1800	15	ThB1+Fe-Ni(5wt.%)-N(5wt.%)-S(20wt.%)	Fine quench crystals+Alloy	-1.14	-1.21	×	n.a.	n.a.	10.70	3.21	58.24	4.86

[a]The experiments were held at 850 °C for 2–12 h before being raised to the target temperature in order to reduce the porosity of graphite capsules and prevent the leakage of the slicate and alloy melta

[b]Mixture of ThB1 basalt and Fe-Ni-N±S alloy (see Table S2)

Glass = Silicate glass, Alloy = Alloy melt, $D^{alloy/silicate}$ = Conc. of C, N or S in alloy melt/Conc. of C, N or S in silicate melt

[c]fO_2 with respect to iron-wüstite buffer (ΔIW) calculated using an ideal solution model for both alloy and silicate melts

[d]fO_2 with respect to iron-wüstite buffer (ΔIW) calculated using a non-ideal solution model for both alloy and silicate melts (See text for details)

fO_2 calculations are made using average values of oxides and metals

1-σ error for $D^{alloy/silicate}$ is calculated by propagating the 1-σ deviation error of C, N or S content in the alloy and silicate melt

n.a. = not applicable

Table S4. Major element compositions (in wt %) of the alloy melts at 1 to 7 GPa.

Exp No.	[a]*n*	Fe	Ni	N	S	C	O	Total
G517-0S	20	90.75	5.45	0.52	0.02	4.53	0.01	101.29
1-σ		0.55	0.10	0.08	0.01	0.39	0.02	0.81
G516-0S	22	89.82	5.58	1.68	0.02	3.88	0.00	100.98
1-σ		0.29	0.13	0.08	0.01	0.16	0.00	0.23
G498-0S	20	89.55	4.58	2.60	0.02	3.11	0.00	99.87
1-σ		0.47	0.08	0.06	0.00	0.15	0.01	0.55
G499-0S	20	88.49	5.62	2.42	0.02	3.64	0.05	100.24
1-σ		0.67	0.38	0.18	0.01	0.24	0.07	0.50
MA176-0S	20	88.11	5.14	3.37	0.04	4.20	0.04	100.90
1-σ		0.36	0.14	0.26	0.02	0.30	0.09	0.79
MA184-0S	20	88.00	3.99	3.02	0.01	3.28	0.62	98.92
1-σ		1.15	0.17	0.17	0.01	0.17	0.36	1.14
G504-10S (S-poor)	25	91.07	4.08	0.42	0.99	3.33	0.19	100.09
1-σ		0.51	0.06	0.08	0.07	0.14	0.03	0.44
G504-10S (S-rich)	25	63.75	4.20	b.d.l.	30.76	0.44	1.11	100.27
1-σ		1.00	0.86		1.40	0.14	0.76	0.59
G503-10S	20	79.49	5.31	1.67	12.18	2.48	0.25	101.38
1-σ		2.36	0.49	0.14	2.39	0.24	0.07	0.51
G493-10S	20	77.88	5.30	2.56	13.94	2.07	0.30	102.05
1-σ		0.43	0.62	0.10	0.78	0.06	0.09	0.45
G496-10S	20	79.75	4.99	2.29	11.97	2.18	0.28	101.46
1-σ		0.82	0.51	0.13	0.83	0.12	0.08	0.37
MA176-10S	20	77.47	4.80	3.37	13.58	1.59	0.33	101.13
1-σ		0.90	0.62	0.21	0.52	0.11	0.17	0.73
MA184-10S	20	75.55	4.70	3.36	14.55	1.64	0.46	100.26
1-σ		1.84	0.46	0.34	1.76	0.24	0.34	1.30
G515-20S (S-poor)	25	90.64	5.22	0.39	1.78	2.89	0.03	100.95
1-σ		0.50	0.09	0.10	0.35	0.33	0.04	0.70
G515-20S (S-rich)	25	63.74	4.54	b.d.l.	32.10	0.19	0.26	100.84
1-σ		1.95	3.06		4.91	0.08	0.22	0.24
G514-20S	20	67.81	5.15	0.74	25.92	0.33	0.85	100.79
1-σ		1.02	1.28	0.18	1.10	0.06	0.22	0.50
G491-20S	20	65.90	6.01	0.91	26.51	0.39	1.07	100.80
1-σ		0.76	1.07	0.10	1.16	0.11	0.51	0.36
G495-20S	15	66.55	4.74	0.95	26.29	0.54	0.63	99.69
1-σ		1.84	1.29	0.14	1.45	0.12	0.52	0.76
MA176-20S	20	66.24	5.77	1.28	25.27	0.35	0.81	99.72
1-σ		1.57	1.09	0.40	3.53	0.04	0.66	0.63
MA184-20S	20	64.03	9.95	1.46	21.97	0.48	0.94	98.84
1-σ		2.40	2.61	0.22	1.42	0.17	0.43	0.80

[a]*n* is the number of measurements averaged to obtain the reported compositions.
b.d.l. = below detection limit
n.a. = not applicable
Si was not detected in any of the experimental alloys.

Table S5. Major element compositions (in wt %) of the silicate melts at 1 to 7 GPa.

Exp No.	[a]*n*	SiO_2	Al_2O_3	Cr_2O_3	FeO	MnO	MgO	CaO	NiO	Na_2O	K_2O	S	N	[a]H_2O	[a]C (ppm)	Total	[b]NBO/T
G517-0S	20/4	49.30	14.60	0.02	11.44	0.22	8.65	11.05	0.01	2.73	0.11	b.d.l	0.03	0.92	300.47	99.13	0.86
1-σ		0.31	0.14	0.01	0.08	0.02	0.09	0.07	0.01	0.05	0.01		0.02	0.08	16.24	0.28	
G516-0S	22/4	47.82	15.33	0.03	12.88	0.22	8.82	10.80	0.01	2.59	0.10	b.d.l	0.07	0.68	270.79	99.39	0.89
1-σ		0.18	0.07	0.01	0.19	0.01	0.07	0.07	0.01	0.03	0.01		0.04	0.06	14.54	0.30	
G498-0S	18/5	45.94	13.87	0.02	13.78	0.21	8.47	10.67	0.01	2.54	0.10	b.d.l	0.09	1.07	311.26	96.82	0.97
1-σ		0.20	0.06	0.01	0.04	0.01	0.04	0.06	0.01	0.04	0.01		0.02	0.07	28.33	0.30	
G499-0S	20/4	48.15	14.56	0.03	13.17	0.21	8.56	10.74	0.02	2.61	0.11	b.d.l	0.19	0.97	651.82	99.39	0.90
1-σ		0.22	0.10	0.01	0.16	0.02	0.06	0.08	0.01	0.07	0.02		0.06	0.06	59.33	0.41	
MA176-0S	20/0	48.70	14.22	0.02	14.43	0.22	7.92	10.65	0.02	2.66	0.09	b.d.l	0.11	n.a.	n.a.	99.03	0.91
1-σ		0.43	0.25	0.01	0.27	0.01	0.16	0.11	0.01	0.05	0.02		0.04			0.39	
MA184-0S	25/0	48.02	13.91	0.03	14.85	0.21	8.79	10.22	0.04	2.44	0.09	b.d.l	0.16	n.a.	n.a.	98.79	0.96
1-σ		0.66	0.16	0.01	0.69	0.02	0.12	0.09	0.04	0.08	0.02		0.05			0.52	
G504-10S	22/4	45.93	15.30	0.03	13.55	0.21	9.05	10.92	0.01	2.59	0.10	0.30	0.03	0.87	252.59	98.92	0.95
1-σ		0.42	0.20	0.01	0.09	0.02	0.17	0.09	0.01	0.05	0.01	0.01	0.03	0.06	23.77	0.86	
G503-10S	20/5	48.33	14.56	0.03	13.14	0.22	8.35	10.59	0.02	2.63	0.11	0.16	0.07	0.87	299.01	99.09	0.89
1-σ		0.13	0.09	0.01	0.06	0.01	0.08	0.05	0.01	0.06	0.01	0.00	0.04	0.06	27.24	0.24	
G493-10S	20/4	46.97	14.92	0.03	13.56	0.22	8.73	10.68	0.01	2.59	0.10	0.11	0.09	0.66	259.24	98.69	0.92
1-σ		0.38	0.15	0.01	0.13	0.01	0.10	0.07	0.01	0.06	0.01	0.00	0.03	0.04	23.74	0.72	
G496-10S	20/4	46.66	14.46	0.03	14.59	0.22	8.27	10.67	0.02	2.57	0.10	0.17	0.15	0.60	542.91	98.57	0.95
1-σ		0.36	0.12	0.02	0.17	0.00	0.09	0.03	0.01	0.05	0.01	0.01	0.05	0.04	50.22	0.72	
MA176-10S	20/0	47.64	14.72	0.03	14.44	0.21	8.30	10.51	0.02	2.51	0.10	0.12	0.14	n.a.	n.a.	98.74	0.91
1-σ		0.61	0.19	0.01	0.17	0.01	0.13	0.10	0.01	0.07	0.02	0.01	0.04			0.57	
MA184-10S	20/0	46.71	14.92	0.03	15.35	0.21	8.47	10.49	0.03	2.40	0.09	0.17	0.16	n.a.	n.a.	99.04	0.95
1-σ		0.42	0.20	0.01	0.22	0.01	0.13	0.14	0.01	0.06	0.01	0.01	0.04			0.57	
G515-20S	25/4	47.01	15.16	0.03	13.36	0.21	8.67	10.58	0.01	2.56	0.13	0.35	0.02	0.78	197.29	98.90	0.90
1-σ		0.45	0.21	0.01	0.20	0.01	0.11	0.07	0.01	0.04	0.01	0.04	0.02	0.07	26.93	0.36	
G514-20S	18/4	40.84	13.89	0.03	12.18	0.18	19.94	9.99	0.02	2.30	0.10	0.22	0.05	0.22	392.98	100.00	1.57
1-σ		0.40	0.38	0.01	0.07	0.01	0.12	0.12	0.01	0.04	0.01	0.01	0.03	0.02	26.46	0.27	
G491-20S	20/5	46.91	12.54	0.01	17.69	0.17	6.84	8.35	0.01	2.06	0.11	0.28	0.06	2.10	339.24	97.16	0.93
1-σ		0.14	0.10	0.01	0.12	0.01	0.08	0.07	0.01	0.05	0.01	0.01	0.02	0.14	30.93	0.47	
G495-20S	20/4	46.45	14.06	0.03	15.57	0.21	7.99	10.38	0.04	2.46	0.12	0.26	0.07	0.85	561.22	98.55	0.97
1-σ		0.27	0.11	0.01	0.39	0.01	0.07	0.09	0.06	0.07	0.01	0.04	0.03	0.07	30.81	0.53	
MA176-20S	20/0	47.58	13.76	0.03	15.75	0.21	7.68	10.27	0.03	2.47	0.10	0.20	0.12	n.a.	n.a.	98.18	0.94
1-σ		0.54	0.33	0.01	0.36	0.01	0.23	0.11	0.01	0.11	0.03	0.01	0.04			0.41	
MA184-20S	20/0	46.86	14.51	0.03	16.03	0.20	8.25	10.30	0.06	2.44	0.09	0.38	0.14	n.a.	n.a.	99.29	0.96
1-σ		0.48	0.16	0.01	0.44	0.02	0.13	0.10	0.04	0.07	0.03	0.02	0.04			0.39	

[a]*n* is the number of measurements averaged to obtain the reported compositions. *n* of 20/4 should be read as 20 spots measured using EPMA and 4 spots measured using SIMS.

[b]NBO/T = (2×Total O)/T - 4, where T = Si + Ti + Al + Cr + P

b.d.l. = below detection limit